Materials Research Express

PAPER

Measuring flow curve and failure conditions for a MEMS-scale electrodeposited nickel alloy ,

To cite this article: D T Read *et al* 2019 *Mater. Res. Express* **6** 0950a6

Materials Research Express

RECEIVED
30 July 2018

REVISED
21 September 2018

ACCEPTED FOR PUBLICATION
8 October 2018

PUBLISHED
26 July 2019

PAPER

Measuring flow curve and failure conditions for a MEMS-scale electrodeposited nickel alloy*,†

D T Read[1], L A Liew[1], R M White[1], N Barbosa[2] and J Geaney[3]

[1] Applied Chemicals and Materials Division, Material Measurement Laboratory, National Institute of Standards and Technology, Boulder CO, United States of America
[2] Material Measurement Laboratory, National Institute of Standards and Technology, Boulder CO, United States of America
[3] U.S. Army RDECOM-ARDEC, United States of America

E-mail: david.read@nist.gov

Keywords: digital image correlation, failure, finite element analysis, LIGA, MEMS, tensile, true strain

Abstract

Implementation of advanced electroplated Ni alloy materials in MEMS-scale mechanisms requires performance predictions that are based on actual, rather than idealized, material properties. Accurate characterization of material properties is necessary to the formulation of material models used in finite element analysis (FEA) simulations that can be relied upon for critical design applications. Quantitative material models, and specifically those implemented in FEA codes, require the use of the true stress-true strain material flow curve as input. Simulations of failure conditions require that a failure criterion be known, such as the failure strain. The subject of this paper is a method for obtaining such characterization of MEMS-scale electroplated materials; it addresses the challenges associated with measurement of stress and, particularly, strain that arise from geometric constraints on MEMS-scale specimens and instrumentation. These include thicknesses a few tenths of a millimeter and below, component dimensions 1 mm and less and planar geometries. A method for refining the material quasi-static flow properties, by inverse-modeling of data from quasi-static tests, is reported. Tests were performed on an electrodeposited nickel alloy by use of a small-scale conventional loading apparatus, with digital imaging to measure specimen displacements. Simulations were carried out using two general purpose, commercially available FEA codes. Inverse modeling was applied to the data to obtain true stress-true strain flow curves. The FEA simulations of the local displacements converged to the experimental results for both commercial codes. Forward-modeling was then used to determine the maximum equivalent true plastic strain in the specimen neck; the calculated values converged to significantly different values in the two codes. This result suggests a need for caution in the use of reported values for maximum effective plastic strain as a failure criterion in FEA simulations.

1. Introduction

Interest in the realization of mesoscale structures with precise geometries and advantageous material properties has been widespread over the last two decades [1]. Mechanical properties of various microscale nickel alloys have been reported [2–5]; these were all fabricated in laboratories, as opposed to commercial sources. Advantageous levels of ductility at high strength, likely resulting from nanocrystalline grain structures, have been reported [6]. However, implementation of advanced electroplated Ni alloy materials in MEMS-scale mechanisms requires effective performance predictions that are based on actual, rather than idealized, material properties during

* Contribution of the U.S. Department of Commerce, National Institute of Standards and Technology. Not subject to copyright in the USA.

† Certain commercial equipment, instruments, or materials are identified in this paper in order to specify the analytical procedure adequately. Such identification is not intended to imply recommendation or endorsement by the National Institute of Standards and Technology, nor is it intended to imply that the materials or equipment identified are necessarily the best available for the purpose. The codes used were ANSYS and ABAQUS; no endorsement or preference is implied.

component design. FEA codes and material models [7, 8] depend on input of the true stress-true strain flow curve [9] of a material for accurate definition of its response to loading. Accessing true stress-true strain behavior throughout a tensile experiment, and in particular at failure, is conventionally performed through the use of round tensile specimens, where the symmetry simplifies the experiment and analysis. Previous reports [10, 11] have described this approach, which includes measurements of both the transverse and longitudinal radii of curvature, followed by application of the Bridgman formula [12–14] or FEA [10] to obtain true strain values, including at failure.

This paper describes the measurement of failure conditions in tension in MEMS-scale specimens of an electrodeposited nickel alloy fabricated by the LIGA technique. LIGA is a German acronym indicating lithography and electrodeposition. The two main measurement issues for this alloy were the rectangular cross sections of the tensile specimens and their small sizes. Specimens were rectangular rather than round because the LIGA process, which involves creating regions bounded by patterned photoresist and then electroplating metal into these regions, is typically used to create structures with rectangular cross sections. The rectangular cross section was an issue because of the lack of an approximation, similar to the widely-used Bridgman approximation for circular tensile specimens [12–14], for the true strain and true stress at the neck of the deforming tensile specimen. Several investigators have reported correction factors deduced from FEA calculations to relate true stress and, in some cases, strain, to experimentally measurable quantities [15–17]. However, reproduction of these methods for the range of effective plastic strain observed in this study produced inconclusive results.

Inverse modeling by use of FEA entails adjusting the material constitutive properties input to the FEA until a sufficiently accurate match is achieved between the FEA output and experimentally measured quantities, thus accomplishing a measurement of the constitutive properties in question [18–20], in particular the flow curve of true-stress against true-strain. This approach was applied in the present effort to MEMS-scale rectangular specimens using two different general purpose, commercially available FEA codes. Forward modeling entails using FEA, with the constitutive properties determined by inverse modeling, to calculate additional quantities correlated with events of interest in the actual experiment. Important among such quantities because of its utility in failure prediction is the maximum effective true plastic strain [21] at failure, which is neither an input to FEA nor experimentally measurable. The subject approach, carried out with general purpose, commercially available FEA codes, was successful provided that details of the analysis must be included in reporting of the parameters for accurate reproduction and use of the results. The objective of this study is to develop and demonstrate a method for measuring the true strain to failure in tension that is applicable to MEMS-scale square and rectangular tensile specimens and is consistent with current FEA methods for device and structural performance prediction.

2. Materials and specimens

Specimens of a Ni-10 Fe alloy were produced by electrodeposition; the microstructure is shown in figure 1. An approximate grain size of 35 nm was obtained from this image using an intercept method [22]. The approach to specimen design was to develop the smallest specimens that could be handled manually, so that no carrier or frame for the specimen was needed. Smaller specimens cannot be handled manually for gripping, and would require more elaborate specimen designs and test procedures, such as the silicon-framed tensile specimen [23] or use of other rigid support substrates [24]. The nominal specimen thickness was 200 μm, with gauge section widths of 200 and 750 μm. These were too small for the attachment of electromechanical extensometers. Digital imaging and digital image correlation (DIC) [25] have in recent decades become widely used for measurements of displacements in mechanical testing, and were used here. Pin grips were chosen for self-alignment and experimental practicality. Specimens of two geometries were fabricated by a commercial supplier [26], using an application of the LIGA process and a final polish. One design, with a square gauge section, is shown in figure 2; the other, rectangular design has similar grip sections, the same thickness, a straight gauge section length of 3 mm, and width 0.7 mm. The width difference from front face to back face over the 200 μm thickness of the specimens was 2 μm. The photolithographic step involved in the LIGA process allowed creation of a gradual 1% taper of the width from 0.202 mm wide at the ends of the center section to 0.200 mm wide in the center of the narrower specimen, as recommended in ASTM Standard Method E8/E8M—15a [27]. The wider specimens were not tapered.

The top surface of each specimen was coated with a thin layer of gold, with 1 μm-thick microfabricated dots deposited and patterned on top of the gold. The dots functioned as fiducial markers for digital image correlation (DIC) [25] used in analyzing the experimental data, as shown in figure 3.

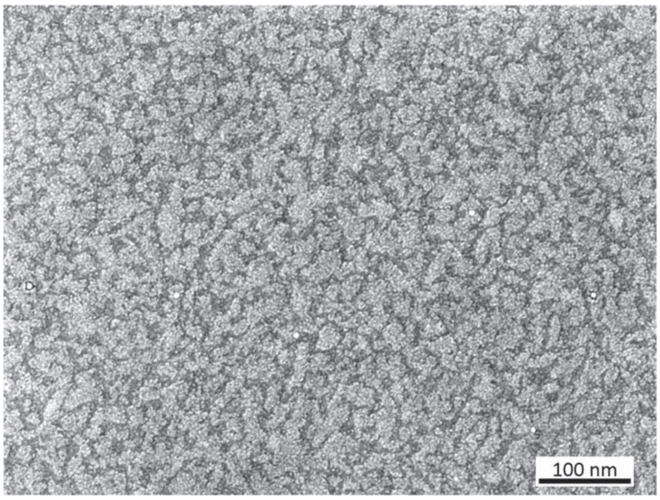

Figure 1. Scanning electron microscope image of the polished and etched surface of the specimen material, showing the microstructure.

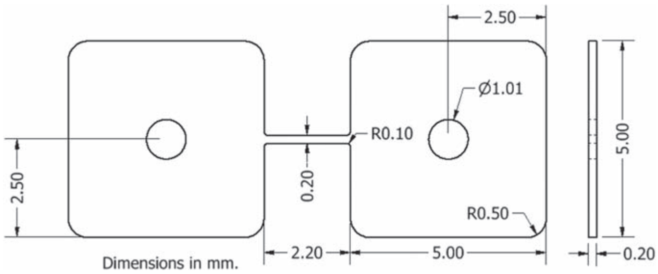

Figure 2. Specimen geometry of MEMS-scale, pin-loaded tensile specimen with square gauge section.

3. Procedures

3.1. Experimental

The specimens were pinned to the clevises; loading was supplied using conventional small-scale test equipment. The nominal strain rate was 0.001 per second. Commercial force sensors with capacities in the 500 N range were used. Their calibrations were checked by dead loading with known weights. The force sensor signal conditioner had a bandwidth of 5 kHz; its output was recorded 5 times per second.

Optical microscopy was used to obtain images at a rate of approximately 1 per 2 s, which produced approximately 100 images in a typical test. Imaging exposure time was approximately 0.5 s. The images consisted of 8-bit grayscales with a resolution of 3072 by 2300 pixels. Displacements were obtained from these by DIC. Subsets 64 pixels square selected from the full images were correlated. For full field measurements, the subset locations were chosen such that the spacing from center to center was one fourth of the subset size. For the engineering strain determination, subsets were selected on opposite ends of the specimen for tabulation of their displacements. The extension of the specimen was the difference in axial displacement between the two ends of the gauge section. The engineering stress was evaluated as the measured tensile force divided by the initial cross-sectional area of the specimen.

3.2. Analytical

The tests were simulated with two different general purpose, commercially available, and widely used FEA codes [7, 8]. Computational effort was reduced by utilizing symmetry and by reducing the modeled size of the specimen grips. The taper in the square cross-section specimens was included in the geometry analyzed. The full version of the square geometry as analyzed is shown in figure 4. The rectangular gauge section geometry is similar, with the same thickness, a straight gauge section width of 0.7 mm and length of 2.7 mm, and radii of curvature of 0.4 mm at the grips.

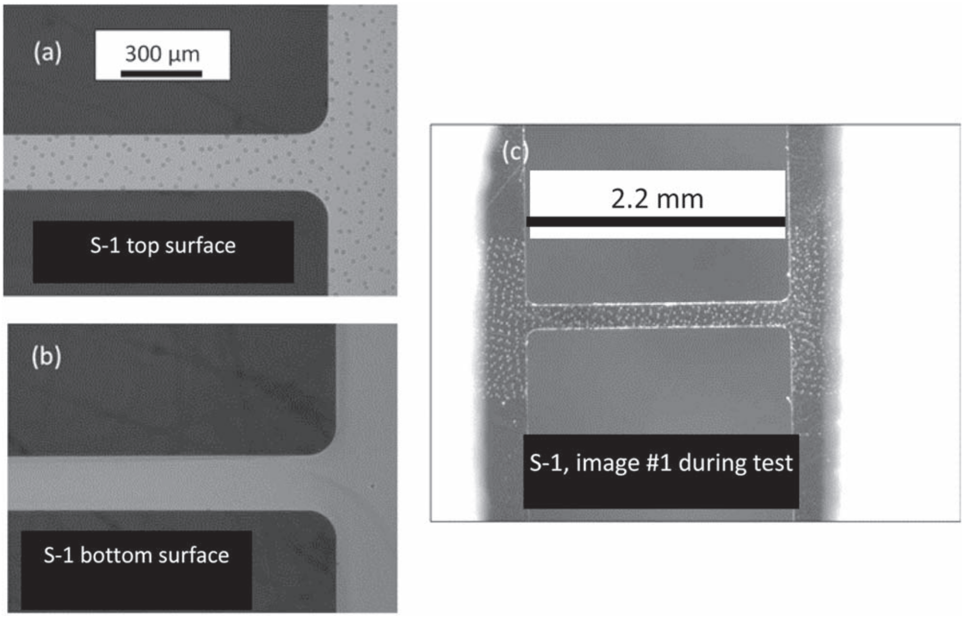

Figure 3. Optical micrographs of a square tensile specimen with microfabricated fiducial markers on the top surface. The gauge width is measured from micrographs similar to those shown in (a) and (b), which were photographed with a 5×-magnification objective lens. (c) is an optical microscope image of the same specimen from the 0.001/s tensile test (objective lens 2×-magnification, oblique illumination).

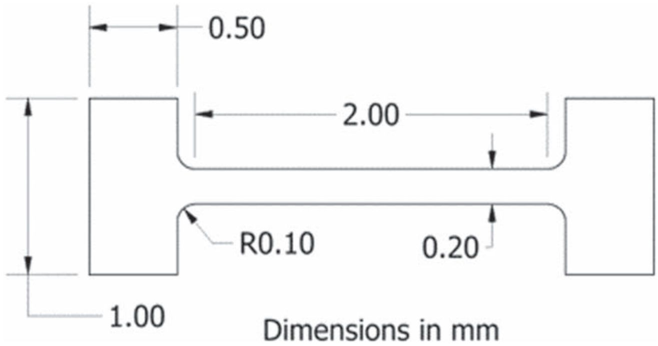

Figure 4. Geometry of the square cross section specimen as analyzed.

4. Inverse- and forward-modeling method

The inverse modeling approach was executed in the following steps:

1. Obtain the initial part of the true stress-strain curve to be input to FEA from the early part of the experimental stress-strain data by applying the usual relationships between engineering strain and true strain and engineering stress and true stress, up to the maximum load [21, 28]. Then extend this to form a complete, although at this point hypothetical, full stress-strain input for FEA.

2. Obtain the experimental post-necking axial strain value at a location outside the neck, denoted below as the *adjacent strain*, from the DIC data at the last image before failure (See figure 6 below). Sets of displacement values measured in each of the two selected regions between the neck and the radii at the ends of the gauge length are fitted, separately, to their corresponding initial locations on the specimen by linear regression. True (logarithmic) strains calculated from the slopes at the opposite ends of the specimen are averaged to obtain the true adjacent strain. This strain value corresponds to the uniform strain discussed by Dieter [9], and its plastic part is constant after necking develops.

3. Model the tensile test by finite element analysis (FEA). Adjust, by trial and error, the input stress-strain curve, obtained in step 1, to meet two criteria: (a) the value of the adjacent strain after necking calculated by

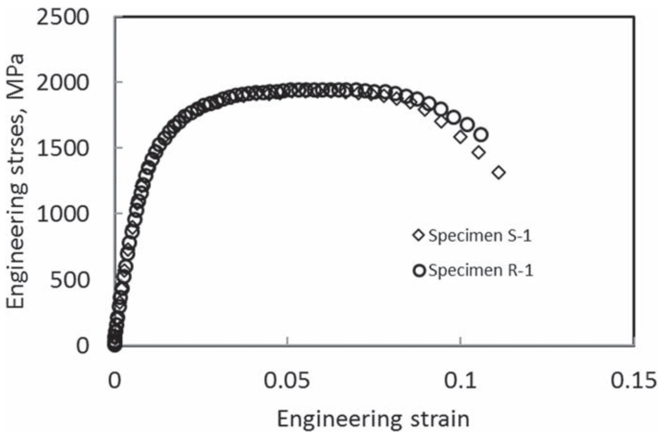

Figure 5. Engineering stress-strain curves of specimens of the square and rectangular geometries, tested at a nominal strain rate of 0.001/s.

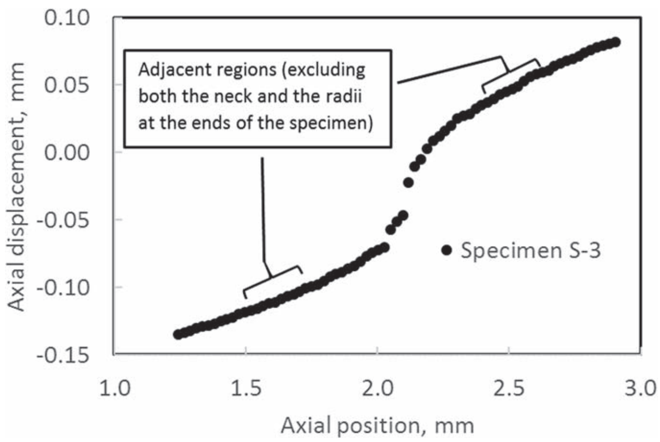

Figure 6. Measured axial displacement plotted against axial position, for square specimen 3. Regions adjacent to the neck are marked.

FEA should be equal to the experimental adjacent strain value, obtained in step 2; and (b) the FEA-calculated engineering stress-strain curve should match the experimental one.

4. Execute a FEA simulation of the deformation utilizing the adjusted input stress-strain curve developed in step 3, and find the FEA step that gives the best agreement between the FEA-calculated axial displacement plotted against initial axial position and the corresponding experimental data obtained from the last image before failure. This FEA step is used for forward-modeling the conditions at specimen failure.

The experimental results used in these steps and the calculations based on them are described in the following two sections.

5. Experimental results

Engineering stress-strain curves for specimens of the two geometries are shown in figure 5. The specimens failed in a ductile manner. The difference between the two curves that appears near failure is similar to the differences seen between different specimens of the same geometry and is not considered further here. The experimental engineering stress-strain curve is the basis of the initial approximation to the true stress-strain curve, as indicated in step 1 of the inverse-modeling, forward-modeling procedure listed above.

A typical example of a set of experimental data for axial displacements as a function of axial position is shown in figure 6. These were obtained from the images acquired during the tensile test, by use of DIC. This data set is used in the remaining steps of the inverse-modeling, forward-modeling procedure listed above. Its key features include the linear regions adjacent to the neck as indicated in the figure, and the amplitude and shape of the rapid increase in displacement through the necked region at the center of the plot. From the regions adjacent to the

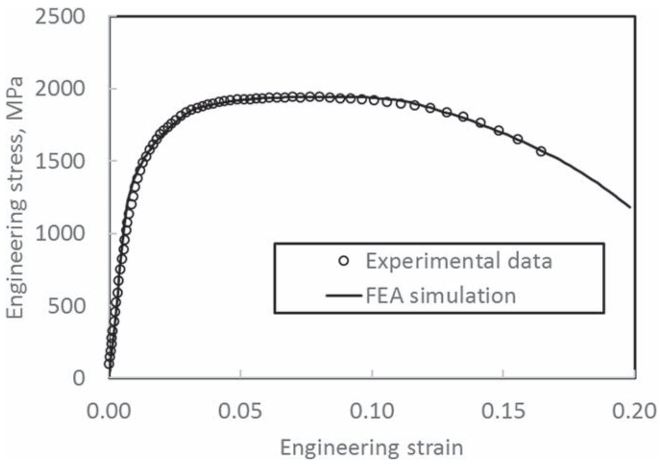

Figure 7. Experimental and FEA-simulated engineering stress-strain curves for rectangular specimen 3. The test was carried out at an engineering strain rate of 0.001/s. The FEA was for quasi-static loading.

neck, values for the axial strain in these regions, here denoted the adjacent strain, can be derived by linear regression. These are used in steps 2 and 3 of the inverse-modeling procedure listed above. The data points that plot out the extent and slope of the increase in displacement through the neck of the specimen are critical in step 4 of the inverse-modeling procedure, because it is the goodness-of-fit between the FEA results and these data that determines which step of the FEA corresponds to the last image before failure. The displacements at the last few data points at the beginning and end are reduced because of the radius at the ends of the gauge section.

6. Inverse modeling

The material true stress-true strain curve was approximated piecewise by up to five expressions of the Ludwik type [29], followed by a region of perfect plasticity. The region of the curve before maximum load was obtained directly from the experimentally-generated results, by converting them to true stress-true strain units by use of the usual formulas [9, 21, 28]. The region after maximum load was adjusted iteratively until both the adjacent strain value and the engineering stress-strain curve produced by the FEA sufficiently replicated the experimentally-generated values.

In this iteration process, the Considère criterion [30] was useful. Ideally, the adjacent strain is equal to the tensile strain value at maximum load in the tensile test [9], because at maximum load necking begins and all further plastic strain occurs in the neck. The Considère criterion [30] states that the strain value at which the force maximum in the tensile test occurs can be determined from the true stress-true strain curve, and that this maximum occurs when the derivative of the true stress with respect to true strain is numerically equal to the true stress. This relationship allowed some anticipation of the effect of adjustments of the input true stress-true strain curve on the FEA-calculated adjacent strain value.

Figure 7 shows the agreement obtained between the FEA-simulated and experimental engineering stress-strain curve for rectangular specimen 3. The root-mean-square (RMS) deviation of the FEA curve from the fitted curve, evaluated at the experimental strain values, is 32.5 MPa, compared to a maximum experimental engineering stress of 1933 MPa.

A similar procedure was used to produce a flow curve for the square specimens. Though both specimens were electroplated on the same wafer, slight differences in the material are possible because of the different geometries of the molds into which the specimens were plated. Figure 8 shows the two flow curves derived by inverse modeling.

The final step in the inverse-modeling procedure is to find the value of the imposed displacement in the FEA simulation that corresponds to the last image acquired before specimen failure. As the displacement in the FEA is imposed as a sequence of small increments, this operation can be re-stated as finding the substep in the FEA simulation of the tensile test that corresponds most closely to the conditions existing at the last experimental image before specimen failure. This was done by comparing the experimentally measured dependence of axial displacement on axial position, as shown above in figure 6, with the values calculated by the FEA simulation. The imposed displacement corresponding to the last image was taken as that which produced the best agreement between the experimental and simulated axial displacement values. The criterion for the best agreement between

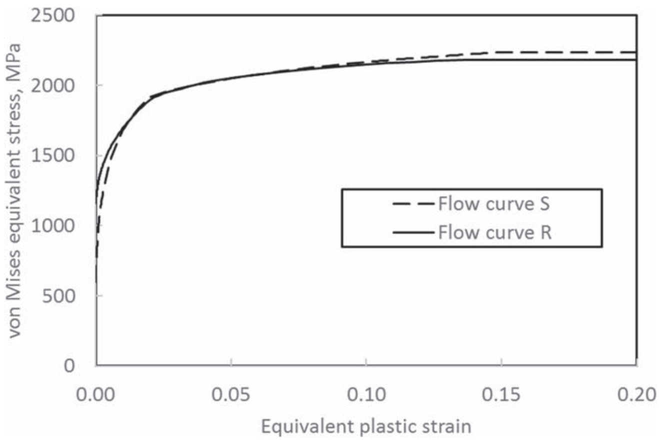

Figure 8. Flow curves determined by inverse modeling for the square and rectangular specimen geometries.

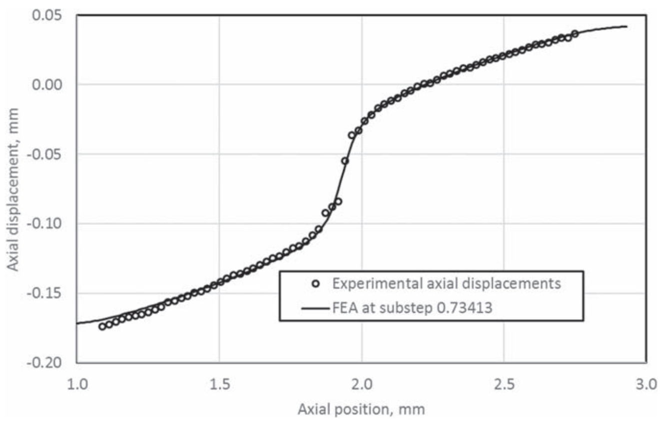

Figure 9. Experimental axial displacement values obtained by DIC for square specimen 1 plotted against axial position and the corresponding FEA-calculated values at the best-matching FEA load increment. The residual differences were summed between axial positions 1.32 and 2.50 mm.

measured and calculated displacement values (step 4, above) was the least sum of squared differences (the least *residual*) over the experimentally sampled axial positions.

The first complication in finding this FEA increment of best agreement was that both the experimentally-measured and FEA-simulated axial displacement values were only available at discrete axial positions, which differed between experiment and FEA. This was handled by tabulating the FEA-simulated displacements at 200 positions along the specimen half-length, and using linear interpolation between the FEA-simulated position values to find the FEA-simulated axial displacement values at the axial position values corresponding to the experimental data.

The second complication was the fact that two important quantities were mis-registered between the experimental images and the FEA results: the zero of axial position and the zero of axial displacement. This mis-registration was caused by the different origins of the coordinate systems between the FEA model and the experimental images. The sought-after residual defined above was sensitive to both of these mis-registrations. To find the proper registrations, the residual at each FEA displacement increment was minimized with respect to both of these zero offsets by applying zero shifts to both. These shifts were calculated using nonlinear regression to minimize the residual difference. This allowed the sought-after residual differences between the experimental results and the FEA simulation to be evaluated independently of the initial mis-registrations.

Figure 9 shows a typical comparison plot of the measured and FEA-calculated axial displacement values plotted against axial position, at a FEA increment near that of minimum residual difference. Figure 10 shows a typical plot of the residual sum of squared differences against the FEA substep, which is proportional to the imposed displacement. For the example in figure 9, the least residual corresponds to a sum of squared differences between FEA-simulation and experimental measurement over 55 experimental axial positions. This corresponds to a root mean square difference of 0.0021 mm at each data point, which is slightly larger than the

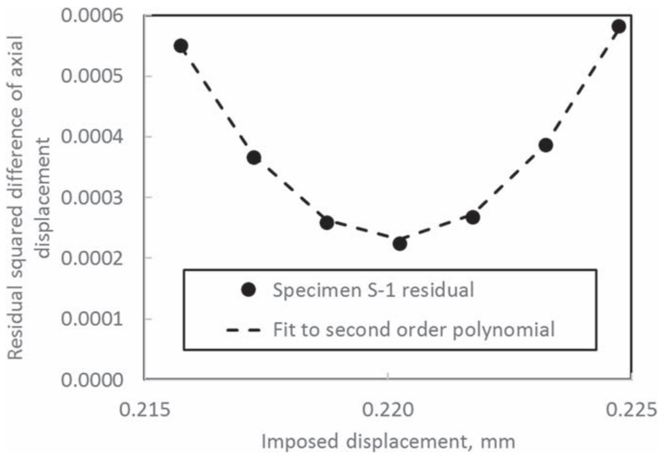

Figure 10. Residual sum of squared differences between FEA-simulated and experimentally-measured axial displacement values for specimen S-1 from the last image before failure, plotted against the FEA imposed displacement.

Table 1. Imposed displacement in tensile test simulation, calculated by inverse modeling by two different analysts using different commercial FEA codes, for the same input data and analysis methods.

Specified maximum element face size in the neck, mm	Square specimen 3, imposed displacement at minimum residual, mm		Rectangular specimen 3, imposed displacement at minimum residual, mm	
	By analyst #1	By analyst #2	By analyst #1	By analyst #2
0.01	0.241	0.226	0.373	0.353
0.016	0.241	0.227	0.373	0.352
0.02	0.241	0.227	0.373	0.352
0.025	0.241	0.228	0.373	0.353
0.035	0.241	0.227	0.374	0.353

spatial resolution of the images obtained from this test, which was 0.0014 mm/pixel. The uncertainty in displacement measurements from the DIC procedure is commonly taken as approximately 0.05 pixel under ideal conditions. The larger differences found here are attributed to non-ideal imaging conditions and to deviations of the actual specimen material and geometry from the ideal assumed in the FEA. It can be seen from the plot in figure 9 that the largest differences occur in the neck, where the strain is highest and is varying rapidly with position, and consequently, where the displacements are most difficult to measure accurately.

Two additional validity checks were performed on the present inverse modeling procedure: (a) dependence on element size; and (b) dependence on FEA software used. The imposed FEA displacements for two tests, one of square specimen 3, and one of rectangular specimen 3, were calculated for different element sizes by two different analysts, each using a different commercially-available FEA code. The element sizes ranged from 0.008 to 0.035 mm. The analysis options that were controlled to be the same between the two analysts included: input true stress-true strain curves (as given above), geometry analyzed, element shape (hexagonal bricks), element order (quadratic), symmetry utilized (eightfold, with some replication at fourfold), deflection assumptions (large), and plasticity model (conventional J_2 plasticity.) The meshes generated by the two FEA codes were both graded, but differed in detail. The results for the displacement imposed on the full tensile specimens are listed in table 1.

The results in table 1 show that the analyses are both well-converged internally. The differences in imposed displacement as calculated by different analysts and codes, which are on average 6% for the square specimens and 5.5% for the rectangular specimens, are attributed to differences in the meshes generated and the differences in the algorithms used between the two codes.

6.1. Application to forward modeling

With known inputs of geometry, material behavior, and imposed displacement, FEA can be carried out to obtain a variety of quantities of interest. Attempts were made to calculate the maximum equivalent true plastic strain in

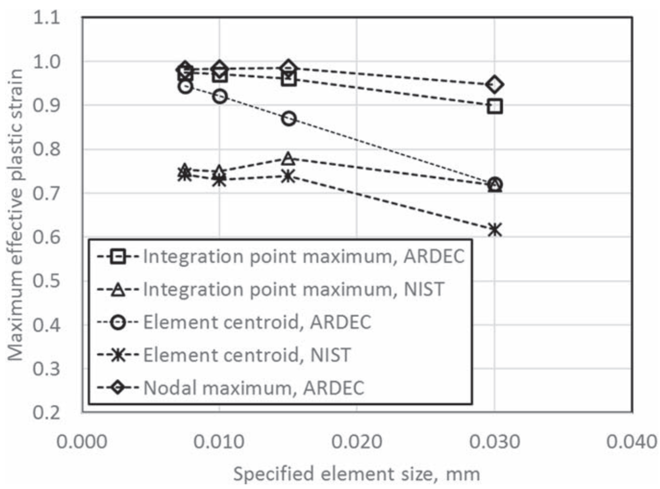

Figure 11. Maximum effective plastic strain for the grip displacement just before failure plotted against specified element size, as calculated by two different widely used finite element analysis codes.

Table 2. FEA results for maximum effective plastic strain at the neck of tensile specimen with square geometry, as shown in figure 3, at the respective imposed displacements listed in table 1, for various specified element sizes and locations, obtained using two different commercially available, general purpose FEA codes.

Specified element size, mm	By analyst #1			By analyst #2		
	Nodal maximum	Integration point	Element centroid	Nodal maximum	Integration point maximum	Element centroid
0.0075	0.981	0.974	0.945	N/A	0.753	0.743
0.01	0.983	0.971	0.922	N/A	0.749	0.731
0.015	0.985	0.961	0.871	N/A	0.779	0.739
0.03	0.947	0.899	0.721	N/A	0.718	0.617

the neck region, corresponding to the imposed displacements at the last image before failure. This quantity is of interest as a possible failure criterion. FEA results for the two commercially supplied general purpose codes used are tabulated in table 2 and plotted in figure 11 for several mesh sizes and analysis options. All are for the converged remote boundary conditions corresponding to the last image before failure for square specimen 3, as listed in table 1. The result was that the calculated values differed significantly between the two FEA codes applied, although both calculations converged convincingly down to a mesh size of 0.008 mm. The values of equivalent plastic strain at the neck of the tensile specimen with square geometry varied from around 0.7 to almost 1.0.

The reporting options available for the code used by analyst #2 did not include the effective plastic strain extrapolated to the nodes. The decrease in effective plastic strain at the element centroid with element size for both analyses occurs because the strain decreases rapidly with distance from the center of the neck, and the element centroid is further from the center of the neck for larger elements. Similar differences between the two codes in the analytical results for effective plastic strain were found for the rectangular geometry.

7. Summary and conclusions

Tensile tests of MEMS-scale specimens of a strong electrodeposited nickel alloy were performed using a conventional mechanical test apparatus, with digital image correlation applied to obtain experimental displacement measurements. Results from two different specimen geometries, one with a square gauge section and one with a rectangular one, were obtained. A procedure for inverse modeling was developed and applied to obtain true stress-true strain curves that differed slightly between the two specimen geometries. Three items of experimental data were used in this process: (a) the engineering stress-strain curve; (b) the axial strain measured outside the neck of the tensile specimen just before failure; and (c) the axial deformation as a function of axial position just before failure. All observed forces, displacements and strains were well-simulated by finite element analysis, using the true stress-true strain curves developed by inverse modeling. Two different analysts using different commercial FEA codes, with the geometries, stress-strain curve inputs, and procedure settings controlled to be the same, calculated nearly equal values of imposed displacement. This demonstrated the validity of the inverse modeling procedure. However, although forward modeling to determine the maximum equivalent true plastic strain in the neck region of specimens at the last image before failure converged for each analysis separately, the two FEA codes produced significantly different results for the maximum effective plastic strain.

These results suggest a need for caution in the use of the maximum effective plastic strain as a failure criterion in FEA simulations. In particular, when quantitative comparison of predicted structural failure conditions to a measured failure criterion is used, the consistency between the methods used in the measurement of the failure criterion and those used in the analysis of the structure should be carefully considered. Analysis practitioners will benefit from future research which documents the results of experiment as well as detailed documentation of the analysis assumptions used for validation of forward modeling results.

Acknowledgments

The authors wish to acknowledge Mr Pasquale Carlucci, US Army RDECOM-ARDEC, for his insight into handling plasticity at material failure, and Mr Charles Robinson, US Army RDECOM-ARDEC, for his review of the manuscript. The authors would like to express their gratitude to Dr M Martin for helpful discussions. Specimen fabrication by Mr Todd Christenson of HT Micro, Inc., was invaluable to this research.

ORCID iDs

D T Read https://orcid.org/0000-0003-1479-1619

References

[1] Bacher W, Menz W and Mohr J 1995 The LIGA technique and its potential for microsystems – a survey *IEEE Trans. Ind. Electron.* **42** 431–41
[2] Sharpe W N, LaVan D A and Edwards R L 1997 Mechanical properties of LIGA-deposited nickel for MEMS transducers *Transducers 97 – 1997 Int. Conf. on Solid-State Sensores and Actuators* Digeset of Technical Papers vol 5 (Chicago)
[3] Buchheit T E, LaVan D A, Michael J R, Christenson T R and Leith S D 2002 Microstructural and mechanical properties investigation of electrodeposited and annealed LIGA Nickel Structures *Metallurgical and Materials Transactions A-Physical Metallurgy and Materials Science* **33** 539–54
[4] Schwaiger R, Reszat J T, Bade K, Aktaa J and Kraft O 2009 A Combined microtensile testing and nanoindentation study of the mechanical behavior of nanocrystalline LIGA Ni-Fe *International Journal of Materials Research* **100** 68–75
[5] Collins J G, Wright M C and Muhlstein C L 2011 Cyclic Stabilization of Electrodeposted Nickel Structural Films *J. Microelectromech. Syst.* **20** 753–63
[6] Sharon J A, Padilla H A and Boyce B L 2013 Interpreting the Ductility of Nanocrystalline Metals *J. Mater. Res.* **28** 1539–52
[7] Dassault Systemes, 'ABAQUS Help,' Dassault Systemes 2016, Abaqus Analysis User's Guide (http://130.149.89.49:2080/v2016/books/usb/default.htm)
[8] ANSYS Incorporated, 'ANSYS Help,' ANSYS Incorporated 2016 Mechanical APDL Theory Reference (https://www.sharcnet.ca/Software/Ansys/16.2.3/en-us/help/ans_thry/ansys.theory.html)
[9] Dieter G E 1986 *Mechanical Metallurgy* 3rd edn (New York: McGraw-Hill)
[10] Johnson G R and Cook W H 1985 Fracture characteristics of three metals subjected to various strains, strain rates, temperatures, and pressures *Eng. Fract. Mech.* **21** 31–48
[11] Clausen A H, Borvik T, Hopperstad O H and Benallal A 2004 Flow and fracture characteristics of aluminum alloy AA5083-H116 as function of strain rate, temperature, and triaxiality *Materials Science and Engineering* A **364** 260–72
[12] Bridgman P W 1944 The stress distribution at the neck of a tension specimen *Transactions of the ASM* **32** 553–74
[13] Bridgman P W 1964 *Studies in Large Plastic Flow and Fracture* (Cambridge: Harvard University Press)
[14] Norris D M Jr, Moran B, Scudder J K and Quinones D F 1978 A Computer simulation of the tensile test *J. Mech. Phys. Solids* **26** 1–19
[15] Zhang Z L, Hauge M, Odegard J and Thaulow C 1999 Determining material true stress-strain curve from tensile specimens with rectangular cross-section *Int. J. Solids Struct.* **36** 3497–516
[16] Scheider I, Brocks W and Cornec A 2004 Procedure for the determination of true stress-strain curves from tensile tests with rectangular cross-section specimens *Journal of Engineering Materials and Technology - Transactions of the ASME* **126** 70–6
[17] Choung J M and Cho S R 2008 Study on true stress correction from tensile tests *Journal of Mechanical Science and Technology* **22** 1039–51
[18] Kajberg J and Lindkvist G 2004 Characterisation of materials subjected to large strains by inverse modelling based on in-plane displacement fields *Int. J. Solids Struct.* **41** 3439–59
[19] Pannier Y, Avril S, Rotinat R and Pierron F 2006 Identification of elasto-plastic constitutive parameters from statically undetermined tests using the virtual fields method *Exp. Mech.* **46** 735–55
[20] Beese A M, Luo M, Li Y, Bai Y and Wierzbicki T 2010 Partially coupled anisotropic fracture model for aluminum sheets *Eng. Fract. Mech.* **77** 1128–52
[21] Lubliner J 2008 *Plasticity Theory* (Mineola, New York: Dover Publications)
[22] ASTM International 2013 *ASTM Standard E112-13, Standard Test Methods for Determining Average Grain Size* (West Conshohocken PA: ASTM International)
[23] Read D T 1998 Tension-tension fatigue of copper thin films *Int. J. Fatigue* **20** 203–9
[24] Neugebauer C A 1960 Tensile properties of thin, evaporated gold films *J. Appl. Phys.* **31** 1096–101

[25] Chu T C, Ranson W F, Sutton M A and Peters W H 1985 Applications of digital-image-correlation techniques to experimental mechanics *Exp. Mech.* **25** 232–44
[26] H T Micro Inc., Albuquerque, NM 2017
[27] ASTM International 2015 *Standard Test Methods for Tension Testing of Metallic Materials* (West Conshohocken, PA: ASTM International)
[28] Lubliner J 2005 Plasticity theory, revised edition [Online]. Available: http://ewp.rpi.edu/hartford/~ernesto/F2008/MEF2/Z-Links/Papers/Lubliner.pdf [Accessed 10 March 2017]
[29] Kleemola H J and Nieminen M A 1974 Strain-Hardening Parameters of Metals *Metall. Trans.* **5** 1863–6
[30] Considère A G 1885 Report on the use of iron and steel in construction *Annales des Ponts et Chaussees* **9** 574–775